Journal of Materials Chemistry A

ROYAL SOCIETY OF CHEMISTRY

PAPER

View Article Online
View Journal | View Issue

Cite this: J. Mater. Chem. A, 2022, 10, 6078

Au single atom-anchored WO_3/TiO_2 nanotubes for the photocatalytic degradation of volatile organic compounds†

Xiaoguang Wang, Honghui Pan, Minghui Sun and Yanrong Zhang *

Received 22nd September 2021
Accepted 29th October 2021

DOI: 10.1039/d1ta08143h

rsc.li/materials-a

Owing to the 100% atom utilization and the high activity, single atom catalysts (SACs) toward photocatalytic oxidation (PCO) represent a promising technology. However, its practical industrial application has been still limited by the complex synthesis methods of the catalyst. Herein, a simple two-step electrochemical approach was developed to synthesize an atomically dispersed Au-loaded WO_3/TiO_2 nanotubes array for volatile organic compounds (VOCs) oxidation. Au atoms were proved to be anchored by oxygen vacancies (OVs) on the WO_3 surface, which significantly enhanced the separation and transfer of photogenerated carriers and the adsorption of toluene, achieving a 95.4% degradation and 85.5% mineralization rate for toluene removal. More importantly, the strong metal-support interaction led to the thermodynamic stability of the Au single atoms, and therefore, the stable toluene degradation cycle was achieved. This work is especially of great industrial significance for application of photocatalytic VOCs removal by SACs technique.

Introduction

Volatile organic compounds (VOCs), widely used in numerous industrial applications (*e.g.*, chemical synthesis, coating and building materials), have become a social and scientific concern as it presents a huge issue that threats the sustainability of ecosystems and human health.[1–3] They can occur in photochemical reactions and cause secondary pollutants, such as $PM_{2.5}$ and ozone. Some of them, such as the benzene series, would trigger the "sick building syndrome", including mucous membrane irritation, headache and fatigue. Furthermore, some of them are known to be carcinogenic.[4] The wise way to control the adverse impact of VOCs is to eliminate them prior to the discharge. Among the existing techniques, such as thermal and catalytic combustion, absorption, biofiltration for eliminating VOCs,[5–7] photocatalytic oxidation (PCO) has attracted much attention due to its low cost and no secondary pollution.[8,9] However, the efficiency and stability of PCO technology still needs to be further improved to meet the practical industrial application.

Single-atom catalysis (SACs) for PCO has emerged as a promising method for the efficient removal of contaminants. The dispersion of isolated metal atoms on the support surfaces provided could maximize the atomic efficiency of precious metals, and minimize the costs associated with the synthesis and utilization of SACs.[10–12] However, originating from the high surface energy of isolated single metal atoms on supports, the metal atom would tend to aggregate, forming clusters or nanoparticles.[13,14] Therefore, appropriate synthetic strategies are essential for the preparation of SACs with these desirable properties. In order to synthesize high-quality SACs, several strategies have been invoked, including (i) designing coordination sites to adsorb and bind metal precursors or metal atoms; (ii) spatially confining single metal atoms into molecular cages; (iii) exploiting defect vacancies in supporting materials to anchor single atom. Among these approaches, the defect vacancies anchoring strategy is considered more prospective due to its universality and operability for metal oxide supports.[15,16] The vacancies could alter the surrounding electronic structure and coordination environment, leading to the appearance of unsaturated coordination sites. These vacancies on supports serve as "traps" to capture metal precursors and anchor metal atoms during post-treatment.[17–19]

Nevertheless, the suboptimal vacancy introduction and single-atom loading method limit the practical application of SACs for VOC removal by PCO. A common method of introducing vacancies to anchor single atoms in metal oxides is assisted thermal treatment at high temperatures under reducing atmosphere (Ar, H_2, $NaBH_4$, *etc.*).[17,20] On the other hand, general approaches for anchoring atomically dispersed metal atoms on vacancy typically employ bottom-up strategies, including atomic layer deposition (ALD), chemical vapor deposition (CVD), mass-selected soft-landing method (MSSL) and wet-chemistry method (*e.g.*, co-precipitation method and impregnation method).[10–12] Obviously, these approaches are

Environmental Science Research Institute, Huazhong University of Science and Technology, Wuhan 430074, China. E-mail: yanrong_zhang@hust.edu.cn

† Electronic supplementary information (ESI) available. See DOI: 10.1039/d1ta08143h

highly infeasible and uneconomical for the scaling-up process of SACs. Therefore, it is essential to develop a simple and easy-to-operate method for anchoring atomically dispersed metals. Recently, a simple electrochemically self-doped approach to introduce oxygen vacancies (OVs) into TiO_2 nanotubes-based compounds was developed in our previous works, by which the quantity and distribution of OVs could be tailored with respect to the duration of the applied cathodic potential.[21,22] This mild electrochemical method makes it possible to introduce OVs to supports on an industrial scale. Moreover, the pulsed electrodeposition approach, which achieves a uniform distribution of loaded species and prevents their agglomeration, has been well established in our earlier works.[23] This approach consisted of a low potential pulse to reduce noble metal ions and a high potential pulse to provide a sufficient relaxation duration to re-establish the concentration equilibrium of precious metal precursors, while the latter could effectively suppress the nucleation tendency of precious metals.[24] These two mentioned methods do not involve the application of high temperature, strong reducing atmosphere and complex equipment. Therefore, bringing the advantages of the electrochemical method to develop single atom photocatalysis is of great practical significance.

In this study, a two-steps electrochemical approach with industrial application prospects was developed to anchor high density Au single atoms on oxygen vacancies of WO_3 in the WO_3/TiO_2 nanotubes composite. Au was selected due to Au susceptibly sparking chemical reactions compared to that of the other metals precious metals according to the indirect relativistic orbital stretching effect (IROSE).[25] Anchoring single Au atoms enhanced the charge-transport, reduced the electron–hole recombination and promoted the adsorption of toluene, thereby demonstrating excellent photocatalytic toluene removal performance. Owing to the increased metal-support interaction of the Au single atoms-anchored WO_3/TiO_2 nanotubes, thermodynamic stability of Au single atoms was achieved, thus ensuring the durability of the POC. Furthermore, the photocatalytic degradation mechanism of gaseous toluene was systematically studied by *in situ* FTIR spectroscopy.

Experimental

Preparation of OVs-W/T

TiO_2 nanotubes (TNTs) were first prepared by an electrochemical anodization technique. Afterward, WO_3 was loaded by an electrodeposition approach (W/T). More details are provided in the ESI.† Then, oxygen vacancies (OVs) were introduced into WO_3/TiO_2 nanotubes (OVs-W/T) by an optimized electroreduction step. The WO_3/TiO_2 nanotubes foil was subjected to a cathodic potential of −1.4 V (*vs.* SCE) in 0.1 M Na_2SO_4 aqueous electrolyte for 600 s under ambient temperature.

Preparation of ^{S}Au-W/T

Single Au atoms were electrochemically loaded on OVs-W/T by the square wave pulse method. The OVs-W/T film was used as the working electrode. The electrolyte solution consisted of 0.1 M NaCl and 2.5 μM $HAuCl_4$. The atomic Au was anchored on OVs by stepping the potential to −0.6 V *vs.* SCE for 5 s, followed by stepping back to −0.2 V for 5 s. The process was repeated for five cycles. The *I–V* curve of the square wave pulse method is shown in Fig. S1.† Subsequently, the as-prepared ^{S}Au-W/T composites were cleaned with deionized water followed by a drying at 60 °C. Au-W/T was the sample obtained by directly depositing Au into the W/T.

Photoelectrochemical measurements

An electrochemical workstation in a three-electrode configuration was used to carry out photocurrent analysis. The prepared composite film with an exposed area of 2 cm × 1 cm served as the photoanode, which was placed with a Pt foil (counter electrode) and an SCE (reference electrode) in a quartz cell containing 0.5 M Na_2SO_4 aqueous electrolyte. The photoanode was irradiated by a 365 nm LED light source. Electrochemical impedance spectroscopy (EIS) was conducted using the same set-up. Further characterization details are provided in the ESI.†

Reactor setup and experimental procedure

The photocatalytic degradation of toluene was carried out in a 15 ml quartz cell reactor with a magnetic bar placed at the bottom of the reactor to circulate air in it. The photocatalyst films were prepared in a dimension of 2 cm × 1 cm. The distance kept between the surface of the photocatalyst and two oppositely placed LED light sources (365 nm) was 1 cm. Before each experiment, the concentration of toluene was adjusted to 160 ppmv by diluting the standard gas (300 ppmv toluene) in the reactor with high-purity air. The concentration of toluene was detected by a gas chromatography instrument equipped with a flame ionization detector (FID).

Results and discussion

Preparation and characterization

The morphological study by field emission scanning electron microscopy (FE-SEM, Fig. 1a and b) clearly showed a highly ordered TiO_2 nanotube array loaded with WO_3 nanoparticles. From the aberration-corrected high-angle annular dark-field transmission electron microscopy (HAADF-TEM), a large number of marked bright points dispersed on the (200) plane of monoclinic WO_3 (Fig. S2†) were observed, confirming the atomic dispersion of Au on ^{S}Au-W/T (Fig. 1c). More HAADF-TEM images of single Au atoms are exhibited in Fig. S3.† According to the inductively coupled plasma atomic emission spectroscopy (ICP) results, the content of Au in ^{S}Au-W/T was 2.41 wt% (Table S1†). As shown in Fig. 1d, due to Ti elemental mapping and its lower brightness caused by weaker Z-contrast,[26] the structure marked with dashed frame was considered as the TiO_2 nanotubes wall. No Au element was observed on the wall, indicating the Au atoms were mainly distributed on the surface of WO_3 nanoparticles rather than TiO_2. Since WO_3 is extremely sensitive to undergo reduction and self-doping, as we reported earlier,[23] electrochemically reduced WO_3 has stronger conductivity compared to TiO_2. Thus, WO_3 was easier to act as an

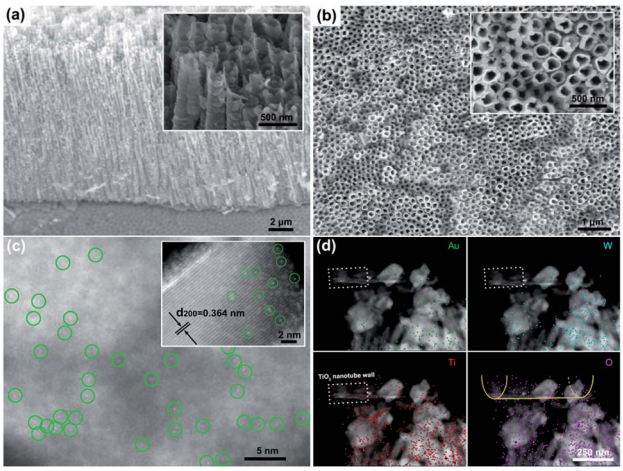

Fig. 1 (a) and (b) FE-SEM image of ^{S}Au-W/T, (c) HAADF-TEM image of ^{S}Au-W/T. Single Au sites are highlighted by green circles. (d) Elemental mappings of the selective HAADF-TEM image of ^{S}Au-T/W. The elemental mappings illustrate the spatial distribution of Au (green), W (blue), and Ti (red), respectively.

electron donor for the reduction of Au^{3+} ions compared to the TiO_2 nanotube walls, which led to Au atoms being preferentially loaded on WO_3 containing a large number of OVs. In sharp contrast, withdrawing the electroreduction step for introducing OVs, with regard to Au-W/T, Au was dispersed on the surface of WO_3 as clusters consisting of several Au atoms due to the lack of anchoring (Fig. S4†).

To clarify the defects and Au state of the prepared samples, electron paramagnetic resonance (EPR) and X-ray photoelectron spectroscopy (XPS) analyses were performed. As seen in Fig. 2a, the EPR spectra exhibited a signal at $g = 2.002$ (3400–3480 G) for OVs-W/T and ^{S}Au-W/T, a characteristic signal of the hole-trapped O^{-}.[27,28] Notably, the OVs signal of ^{S}Au-W/T was

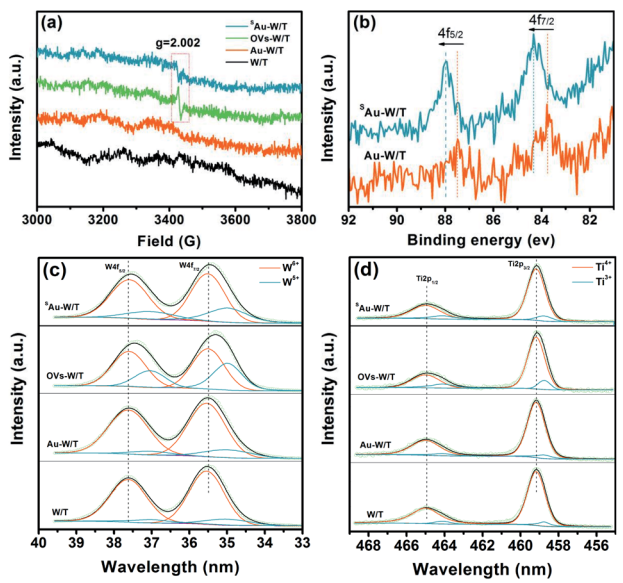

Fig. 2 (a) EPR spectra of samples. (b) Au 4f, (c) W 4f and (d) Ti 2p XPS spectra of the samples.

weaker than that of its precursors, *viz.*, OVs-W/T, giving strong evidence for anchoring Au on OVs. Owing to the bonding of the Au atoms with the W^{5+} near OVs, the unpaired electrons content decreased upon the square wave pulse step for anchoring Au, bringing about the decline of the OVs signal intensity.[17,18,29] The XPS peaks of Ti 2p, W 4f, O 1s and adventitious carbon were found in all samples, and the XPS Au 4f peaks could be observed in ^{S}Au-W/T and Au-W/T (Fig. S5†).[26] Notably, as seen in Fig. 2b, the XPS Au $4f_{5/2}$ and $4f_{7/2}$ binding energies of ^{S}Au-W/T positive shifted to higher energy values compared with that of Au-W/T. The high energy shift can be explained by an electrostatic final state effect. According to the electrostatic drop model, the ionization energy of a spherical metal droplet increases linearly as a function of the inverse cluster radius $1/R$ according to $IP = IP(bulk) + \alpha e^2/4\pi\varepsilon_0 R$, where IP is the ionization potential and α represents a constant.[17] Thus, the upshift in the binding energy indicated the smaller Au particle size of ^{S}Au-W/T compared to that of Au-W/T, which further implied the atomic dispersion of Au. The W 4f XPS spectra (Fig. 2c) exhibited two broad peaks, the W $4f_{7/2}$ located at 35.5 eV and the W $4f_{5/2}$ located at 37.6 eV. The Ti 2p XPS spectra also showed two characteristic peaks, *viz.*, Ti $2p_{3/2}$ and Ti $2p_{1/2}$ centered at about 459.1 and 464.9 eV (Fig. 2d). Compared to the pristine W/T, the W 4f and Ti 2p peaks of the OVs-W/T sample negatively shifted obviously, which confirmed the formation of and W^{5+} and Ti^{3+}.[21,30] The W 4f and Ti 2p peaks of the ^{S}Au-W/T and Au-W/T also showed varying degrees of shift change, indicating the change of the W^{5+} and Ti^{3+} relative amounts.

To figure out the relative amounts of different oxidation states of Ti and W, the XPS spectra of Ti 2p and W 4f were strictly deconvoluted into their corresponding two doublets, *i.e.*, the former as W^{5+} and W^{6+} and the latter as Ti^{3+} and Ti^{4+}.[31,32] As shown in Tables S2 and S3,† OVs-W/T showed the highest W^{5+} and Ti^{3+} concentration, up to 36.0% and 16.7%, respectively. The existence of OVs could be understood by the presence of W^{5+} and Ti^{3+} so as to meet the charge neutrality.[33,34] Notably, the W^{5+} concentration of ^{S}Au-W/T was found to be significantly lower than that of OVs-W/T, which indicated the electron transfer from W^{5+} near the OVs to the Au single atom anchored at the OVs. Also, a very small decline of the Ti^{3+} concentration in ^{S}Au-W/T implied that almost no Au atoms were anchored on the OVs of TiO_2. Whereas in the case of Au-W/T, the content of W^{5+} and Ti^{3+} was similar to that of the W/T due to the absence of OVs, as well as anchored Au atoms, which was identical with the EPR results.

The extended X-ray absorption fine structure (EXAFS) was measured to further clarify the single-atom state and distribution of Au. Fig. 3a presents the W L_3-edge X-ray absorption near edge structure (XANES) spectra of ^{S}Au-W/T, OVs-W/T, and a monoclinic WO_3 reference. The major features of the W L_3-edge XANES spectra first negatively shifted by the introduction of oxygen vacancies, indicating the formation of the lower valence species, *i.e.*, W^{5+}. Then, it positively shifted by anchoring Au atoms, which again indicated a partial transformation of the W^{5+} to W^{6+}. Moreover, the Fourier transformation at the R space was conducted for the EXAFS (FT-EXAFS) and different peaks were observed in Fig. 3b. The first

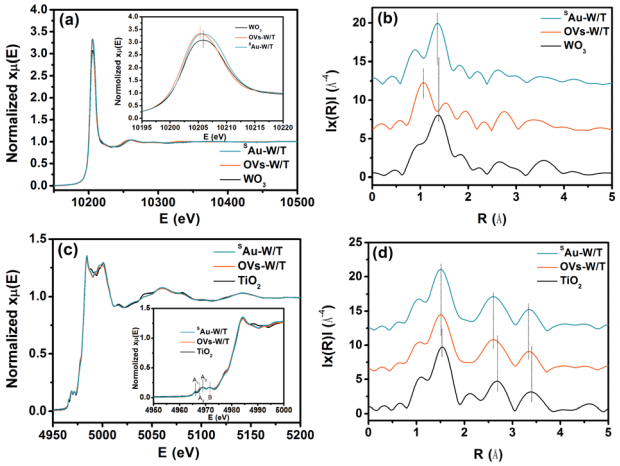

Fig. 3 (a) Normalized XANES spectra and (b) Fourier transforms of the EXAFS at the W L_3-edge. (c) Normalized spectra and (b) Fourier transforms of EXAFS at the Ti K-edge.

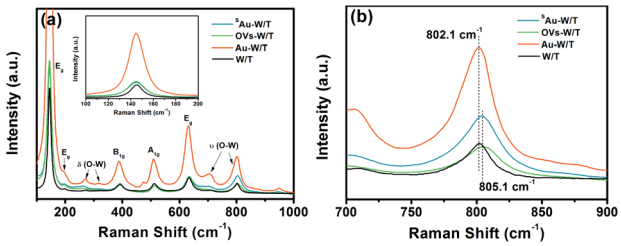

Fig. 4 (a) Raman spectra and (b) the change of W–O stretching modes of WO_3 of samples.

peak, in the distance interval of 0.8–1.9 Å, was attributed to the first distorted shell containing 6 oxygen atoms. The second (2.3–3.1 Å) and the third (3.2–4 Å) were attributed to multiple scattering processes within the first shell of the WO_6 octahedra and the first W–W coordination shell, respectively.[35] The distance interval of the peaks could represent the length of the bond corresponding to their attribution. Obviously, by introducing OVs, the W–O bond (R = 1.0 Å) of OVs-W/T was notably shortened, compared to that (R = 1.38 Å) of W/T. During the electrochemical reduction process, the stable monoclinic WO_3 would form H_xWO_3 with smaller cell parameters by proton insertion into the WO_3 lattice, while generating W^{5+} and OVs, which led to a shortening of the W–O bond length. Moreover, by anchoring single Au atoms, the first peak of ^{S}Au-W/T shifted up to 1.32 Å. This was due to the Au atoms occupying the oxygen vacancy and bonding to its nearby atoms, elongating the W–O bond. For the Ti K-edge XANES spectra (Fig. 3c), the major features of the four pre-edge XANES (*i.e.*, A_1, A_2, A_3 and B) originated from induced electronic transitions from the hybridization orbitals of TiO_2, in which the three A peaks were dominantly from the hybridization of the 3d–4p orbitals, while the B peak belonged to 1s transitions to the t_{2g} and e_g bands.[36] As shown in Fig. 3d, three major Fourier-transform peaks appeared. The FT peak at 0.9–2.0 Å corresponded to the single scattering path of Ti → O by six-coordinated oxygen nearest neighbors around the Ti atom. The peaks at 2.5–3.0 and 3.0–4.0 Å were assigned to single scattering by the edge-shared octahedra and corner-shared octahedra, respectively, and both of them were due to the single scattering path of Ti → Ti by neighboring Ti atoms.[37] Notably, introducing OVs also resulted in a shortening of the Ti–O bond, while anchoring single atoms did not lead to a change in the TiO_2 bond length, which again indicated that the Au atoms were mainly distributed on WO_3 rather than TiO_2.

The formation of OVs and single Au atoms was further monitored by Raman spectroscopy. As seen in Fig. 4a, all samples exhibited 9 peaks, in which 5 were for anatase TiO_2 and 4 for WO_3. The peaks at 272, 326 cm^{-1} belonged to W–O bending modes [δ(O–W)] of the bridging oxygen, and the peaks at 708 and 806.5 cm^{-1} were assigned to the W–O stretching modes [ν(O–W)].[32,38] The rest of the peaks were assigned to the E_g, A_{1g} and B_{1g} modes of TiO_2.[21] Evidently, the Raman signal intensity of Au-W/T was much higher than that of the other sample, which was attributed to the localized surface plasmon resonance (LSPR) effect of Au clusters. Under illumination, photo-induced electrons were generated from the nano-size Au. Then, they migrated to WO_3 and TiO_2, and inelastically collided with the electrons presented there. This promoted the vibration of W–O and Ti–O, and thus enhanced the surface Raman scattering.[39] Nevertheless, LSPR of noble metals strongly depends on the cluster size.[40] The LSPR effect of nano-scale Au is mainly because of intraband transitions between the outermost electrons within the Au 6s 1p hybridized atomic orbitals.

Meanwhile, the single Au atoms lack interband-transition and conduction electrons of Au, resulting in inability to arouse LSPR. Thus, the similar intensity of the δ(O–W) and ν(O–W) Raman peaks belonging to ^{S}Au-W/T and W/T suggested the lack of Au clusters and nanoparticles. Furthermore, the peaks assigned to WO_3 underwent an upshift by introducing OVs and anchoring Au atoms. For instance, the ν(O–W) peak with the strongest signal intensity shifted from 802.1 cm^{-1} to 805.1 cm^{-1} (Fig. 4b), which can be interpreted as the shortening of W–O bonds due to the introduction of OVs,[21] consistent with the EXAFS results.

In general, the incorporation of OVs and metal species on the surfaces of semiconductor materials could improve their optical absorption, carrier separation and transfer, and thus the photoelectric performance.[12,21,26] As seen in Fig. 5a, owing to the defect energy level by incorporating the OVs, the absorption edge of OVs-W/T red shifted.[32,41] Moreover, owing to the LSPR effect, Au-W/T exhibited enhanced absorption in the visible and NIR regions. Likewise, the similar light absorption exhibited by ^{S}Au-W/T and W/T again indicated the absence of the Au cluster in ^{S}Au-W/T. The EIS study was carried out to characterize the interfacial resistance of the samples. As seen in Fig. 5b, a smaller semicircle was observed for the ^{S}Au-W/T compared to the W/T, indicating a reduced charge transfer resistance by anchoring Au atoms. In general, surface OVs and single metal atom facilitate the charge carrier separation due to the unsaturated property,[10,21] while the enhanced carrier transfer property can promote the spatial separation of photogenerated electrons and holes,[42,43] which definitely contributes to the

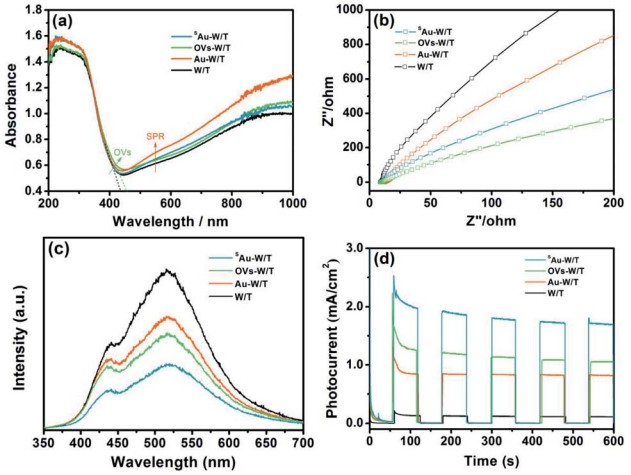

Fig. 5 (a) DRS, (b) EIS, (c) PL and (d) photocurrent responses of samples.

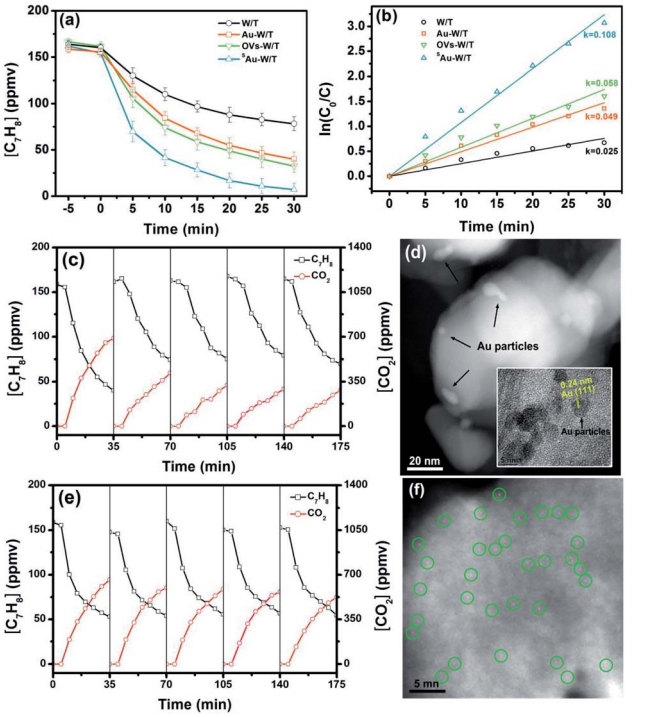

Fig. 6 (a) Photodegradation of toluene by samples and (b) pseudo first-order kinetic curve. (c) Recycle tests and (d) HAADF-TEM image of Au-W/T after the recycle; the insert is the TEM image of Au-W/T. (e) Recycle tests and (f) HAADF-TEM image of ^{S}Au-W/T after the recycle.

improvement of the photoelectric performance. As seen in Fig. 5c, the PL spectra of the samples showed two fluorescence peaks. The peak at 450 nm was due to self-trapped excitons, and the peak at 530 was ascribed to the recombination of trapped holes (such as OVs). Introducing OVs, the PL signal of the OVs-W/T recorded using excited light of 320 nm weakened. Subsequently, anchoring Au atoms on OVs-W/T, the PL signal intensity of ^{S}Au-W/T further declined, indicating the significantly improved carrier separation. Consequently, compared with W/T, a 17-time higher photocurrent, up to 1.8 mA cm^{-2}, was achieved from the ^{S}Au-W/T, corresponding to an incident photon-to-current conversion efficiency (IPCE) of 11.34% (IPCE values are summarized in Table S4†), which indicated that the separation efficiency of photoinduced electrons and holes was improved.[44,45]

Photocatalytic toluene degradation and mechanism

To compare the PCO activity of VOCs by the prepared samples, gaseous toluene was used as a model pollutant and subjected to the photocatalytic degradation. For every experimental run, the adsorption equilibrium of the composite and the pollutant was achieved by mixing them for a specified period, prior to the irradiation step of the photocatalytic system. As shown in Fig. 6a and b, under 365 nm irradiation from an LED source, a dramatic difference in the degradation kinetics of toluene was found for the prepared samples. The degradation efficiencies (DE) achieved in a period of 30 min by W/T, Au-W/T, OVs-W/T and ^{S}Au-W/T were 51.1%, 74.3%, 79.9% and 95.4%, respectively ($DE_{toluene} = ([C_7H_8]_{0\ min} - [C_7H_8]_{60\ min})/[C_7H_8]_{0\ min} \times 100$). Anchoring Au atom on the OVs of W/T significantly improved the degradation of toluene. The reaction kinetic rate of ^{S}Au-W/T was 0.108 min^{-1}, 4.3-fold higher than that of W/T. The variation in the efficiency of the photocatalytic removal of toluene for the prepared samples was identical with the trend of the photocurrent density.

One major concern for SAC is a substantial tendency for single atoms to aggregate due to their high surface energy, resulting in thermodynamic instability.[10,13,14] As shown in Fig. 6c, on directly loading the Au species on W/T without OVs, the degradation performance of toluene by Au-W/T obviously deteriorated after one recycle experiment. After 5 cycles, its toluene degradation efficiency (DE) and the mineralization efficiency (ME) decreased from 74.3% and 63.3% to 56.7% and 25.2%, respectively. The deterioration was attributed to the decrease in the number of metal active centers caused by the aggregation of Au atoms. As shown in Fig. 6d, after the recycle experiment, the Au cluster consisting of a few atoms was aggregated into particles with a size of 2–5 nm. In sharp contrast, an excellent durability of degraded toluene by ^{S}Au-W/T during the recycle experiments was observed in Fig. 6e. Since Au atoms were anchored on OVs of W/T to achieve their thermodynamic stability, the aggregation tendency of single Au atoms was suppressed, which could be confirmed by the atomic dispersion of Au after the 5 recycle experiments, as shown in Fig. 6f. To further explore the possible intermediate species and the detailed toluene oxidation mechanism over ^{S}Au-W/T, *in situ* FTIR spectra were collected under 365 nm light irradiation (Fig. 7). Prior to light irradiation, toluene was adsorbed for 6 minutes to reach adsorption equilibrium on the surface. After the photocatalytic reaction, the bands at 2360 and 2341 cm^{-1} (Fig. 7c) corresponding to CO_2 increased as the reaction proceeded, and some new IR features at 3750–3600 and 1700–1450 cm^{-1} were formed (Fig. 7b and d). A summary of the assigned IR modes to different functional groups is given in Table S5.†[46–49] Among them, the bands at 1610, 1599, 1500 and

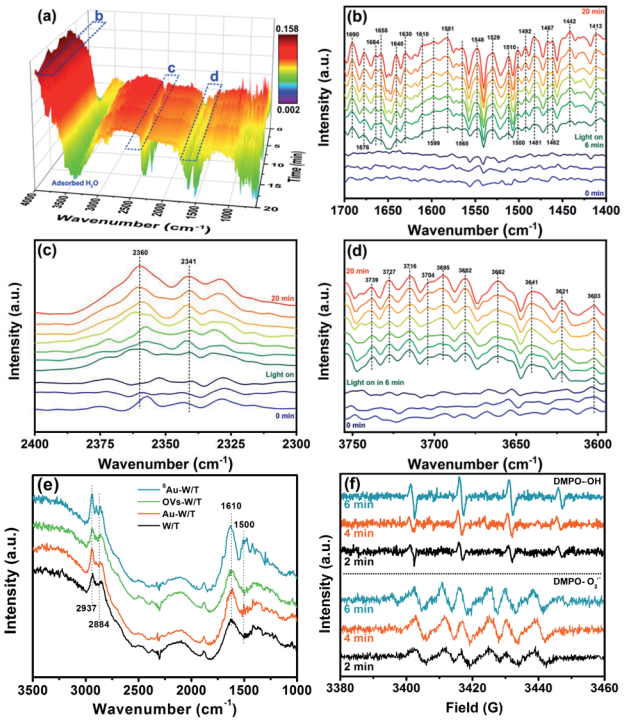

Fig. 7 (a)–(d) *In situ* FTIR spectra of gaseous toluene degradation process by ^{S}Au-W/T under 365 nm light irradiation. The time interval for the FTIR spectrum is 2 min. (f) Steady-state FTIR spectra of the different samples in toluene vapor. (e) EPR spectra of DMPO-·OH and DMPO-O_2·$^-$. ODMPO-O_2·$^-$ was determined in a methanolic solution.

1492 cm^{-1} were assigned to the skeleton stretching and bending vibrations of the aromatic ring. The bands at 1467 and 1462 cm^{-1} were attributed to the C–O stretching vibration of benzyl alcohol. The bands at 1690 and 1676 cm^{-1} were associated with the stretching vibration of aldehydes, indicating the formation of benzaldehyde. The bands located at 1565, 1548 and 1529 cm^{-1} were assigned to the asymmetric stretching vibration of the carboxylate group from the benzoic acid species. The bands at 1581 and 1481 cm^{-1} were due to the C=C stretching vibration of benzoic acid. The one at 1658 cm^{-1} was assignable to the *p*-benzoquinone-type species. Moreover, IR modes related to some small molecule species were observed. The band at 1413 cm^{-1} was due to the C=O stretching vibrations of saturated aliphatic acids (formate and acetate). The bands at 1510 and 1442 cm^{-1} are assigned to the C=O stretching vibrations and COO– stretching vibration of the maleate species, respectively, which could be produced by the catalytic oxidation of generated intermediate compounds during the degradation process. In addition, the bands at 1640 and 1630 cm^{-1} corresponding to the surface water species were observed in the FTIR spectra. The bands appearing in the range of 3750–3600 cm^{-1} were related to hydroxyl groups on the catalyst surface (Fig. 7d). The characteristic bands of the surface hydroxyls at 3695, 3682, 3662, 3641, 3603 cm^{-1} corresponded to the bridged –OH group. The band at 3621 cm^{-1} could be attributed to the O–H bending and stretching vibrations of carboxylic acids. Moreover, the bands at 3739, 3727, 3716 and 3704 cm^{-1} are assigned to the O–H stretching vibration of the terminal hydroxyls, which could further produce ·OH radicals by the reaction between the photo-generated holes and the adsorbed hydroxyls species.

Moreover, to clarify the effect of anchored Au on toluene adsorption, steady-state FTIR characterization for the different samples was carried out in toluene vapor. As shown in Fig. 7e, the FTIR peaks of ^{S}Au-W/T corresponding to the skeleton stretching and bending vibrations of the aromatic ring (1610 and 1500 cm^{-1}) and the C–O stretching vibration mode of aromatic ring (2937 and 2884 cm^{-1}) showed much higher intensity than that of other samples, indicating that ^{S}Au-W/T adsorbed more toluene. Since single metal centers have an unsaturated nature, the single Au sites would promote the adsorption of substrate molecules as widely reported,[10–12] which undoubtedly facilitates the photocatalytic reaction process, including the formation of strong oxidative free radicals. As shown in Fig. 7e and f, the EPR results demonstrated the generation of ·OH, as well as O_2·$^-$ radical species, both of which were crucial in the PCO reaction according to the quenching experiment over ^{S}Au-W/T (Fig. S6†).

To clarify the transfer mechanisms of photogenerated carriers and generation of the ·OH and O_2·$^-$ over the ^{S}Au-W/T, the ultraviolet photoelectron spectroscopy (UPS) measurements were carried out to ascertain the band structures (Fig. S7†). The conduction band (CB) and valence band (VB) potentials of electrochemically reduced TiO_2 were about −0.56 and 2.61 eV, respectively, while two of the electrochemically reduced WO_3 were about 0.12 and 2.90 eV, respectively. Notably, the CB potential of TiO_2 is sufficiently negative to reduce O_2 into O_2·$^-$, while the CB potential of WO_3 is more positive than the potential of O_2·$^-$/O_2. Thus, O_2·$^-$ should be produced by the CB of TiO_2 rather than the CB of WO_3, which followed the Z-scheme as widely reported about WO_3/TiO_2 heterojunction.[50–54] The greater work function of WO_3 than that of TiO_2 leads to forming a built-in electric field that is directed from TiO_2 to WO_3 when their Fermi levels reach equilibrium. Consequently, the electron transfer occurs from the CB of WO_3 to the VB of TiO_2, resulting

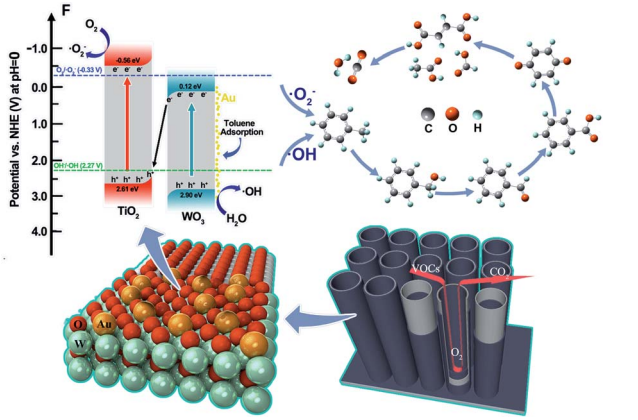

Scheme 1 Schematic mechanism for gaseous toluene degradation over the ^{S}Au-W/T.

in aggregation of photogenerated electrons and holes in the CB of WO_3 and VB of TiO_2, respectively.

Based on the above results and analysis, as shown in Scheme 1, a PCO mechanism of gaseous toluene by ^{S}Au-W/T was proposed. The transfer mechanisms of photogenerated carriers over the WO_3/TiO_2 heterojunction followed the *Z* direction. Anchoring Au atoms on the OVs of WO_3 significantly improved the separation and transfer of photogenerated carriers, which promoted the production of the $^{\bullet}OH$ and $O_2^{\bullet-}$. In addition, anchoring Au significantly promoted toluene adsorption due to the construction of unsaturated coordination sites, which facilitated these radicals to attack the methyl group of toluene, generating benzyl alcohol, benzaldehyde and benzoic acid. With further oxidation, the *p*-benzoquinone-type species and its ring-opening products (such as formate, acetate and maleate), were obtained, which were eventually mineralized into CO_2 and H_2O.

Conclusion

In summary, atomically dispersed Au anchored by surface OVs of WO_3 in WO_3/TiO_2 nanotubes was constructed, exhibiting a 1.8 mA cm^{-2} photocurrent, 17 times than that of the pristine WO_3/TiO_2 nanotubes, and the highest efficiency in degrading toluene. The enhancement in performance was ascribed to the significantly improved carrier transport and separation, as well as toluene adsorption. Furthermore, owing to the support-single metal atom strong interaction due to the anchoring by OVs, thermodynamic stability of Au atoms was achieved, resulting in the durability of VOCs degradation. Importantly, the entire fabrication steps, including the doping of OVs and anchoring of Au atoms, were based on electrochemical approaches. No practices of high temperature and reduced atmosphere were involved, which is highly viable and advantageous for the large-scale synthesis of SACs and practical application of SACs for PCO of VOCs.

Author contributions

Xiaoguang Wang: conception, experimental investigation, manuscript writing, graphic visualization; Honghui Pan: data curation, experimental investigation; Minghui Sun: experimental investigation, graphic visualization; Yanrong Zhang: conception, resources, project administration, funding acquisition.

Conflicts of interest

The authors declare no competing interests.

Acknowledgements

This work partially was supported by the National Key Research and Development Program of China (No. 2020YFC1908704), the National Natural Science Foundation of China (52070082), the International Science & Technology Cooperation Program of Hubei Province (2020BHB023), and the International Science & Technology Cooperation Program of China (No. 2016YFE0126300). The authors thank the Analytical and Testing Center of HUST for the use of the Raman, SEM, TEM and XPS analysis facilities.

Notes and references

1 A. H. Mamaghani, F. Haghighat and C.-S. Lee, *Appl. Catal., B*, 2017, **203**, 247–269.
2 J. Li, G. Zhang, W. Cui, W. Cen, Z. Wu, S. Lee and F. Dong, *J. Mater. Chem. A*, 2019, **7**, 3366–3374.
3 Z. Jiang, X. Feng, J. Deng, C. He, M. Douthwaite, Y. Yu, J. Liu, Z. Hao and Z. Zhao, *Adv. Funct. Mater.*, 2019, **29**, 1902041.
4 D. Tobaldi, D. Dvoranová, L. Lajaunie, N. Rozman, B. Figueiredo, M. Seabra, A. S. Škapin, J. Calvino, V. Brezová and J. Labrincha, *Chem. Eng. J.*, 2021, **405**, 126651.
5 P. Wu, X. Jin, Y. Qiu and D. Ye, *Environ. Sci. Technol.*, 2021, **55**, 4268–4286.
6 H. Rajabi, M. H. Mosleh, T. Prakoso, N. Ghaemi, P. Mandal, A. Lea-Langton and M. Sedighi, *Chemosphere*, 2021, **283**, 131288.
7 M.-F. Han, X.-R. Hu, Y.-C. Wang, Z. Tong, C. Wang, Z.-W. Cheng, K. Feng, M.-M. Qu, J.-M. Chen and J.-G. Deng, *Crit. Rev. Environ. Sci. Technol.*, 2020, 1–31.
8 R. Chen, J. Li, H. Wang, P. Chen, X. a. Dong, Y. Sun, Y. Zhou and F. Dong, *J. Mater. Chem. A*, 2021, **9**, 20184–20210.
9 H. Ren, P. Koshy, W.-F. Chen, S. Qi and C. C. Sorrell, *J. Hazard. Mater.*, 2017, **325**, 340–366.
10 C. Gao, J. Low, R. Long, T. Kong, J. Zhu and Y. Xiong, *Chem. Rev.*, 2020, **120**, 12175–12216.
11 F. Zhang, Y. Zhu, Q. Lin, L. Zhang, X. Zhang and H. Wang, *Energy Environ. Sci.*, 2021, **14**, 2954–3009.
12 S. K. Kaiser, Z. Chen, D. Faust Akl, S. Mitchell and J. Pérez-Ramírez, *Chem. Rev.*, 2020, **120**, 11703–11809.
13 Y. Zhao, W. J. Jiang, J. Zhang, E. C. Lovell, R. Amal, Z. Han and X. Lu, *Adv. Mater.*, 2021, 2102801.
14 K. Qi, M. Chhowalla and D. Voiry, *Mater. Today*, 2020, **40**, 173–192.
15 L. Wang, W. Chen, D. Zhang, Y. Du, R. Amal, S. Qiao, J. Wu and Z. Yin, *Chem. Soc. Rev.*, 2019, **48**, 5310–5349.
16 S. Ding, H.-A. Chen, O. Mekasuwandumrong, M. J. Hülsey, X. Fu, Q. He, J. Panpranot, C.-M. Yang and N. Yan, *Appl. Catal., B*, 2021, **281**, 119471.
17 J. Wan, W. Chen, C. Jia, L. Zheng, J. Dong, X. Zheng, Y. Wang, W. Yan, C. Chen and Q. Peng, *Adv. Mater.*, 2018, **30**, 1705369.
18 X. Hu, J. Song, J. Luo, H. Zhang, Z. Sun, C. Li, S. Zheng and Q. Liu, *J. Energy Chem.*, 2021, **62**, 1–10.
19 X. Wu, H. Zhang, S. Zuo, J. Dong, Y. Li, J. Zhang and Y. Han, *Nano-Micro Lett.*, 2021, **13**, 1–28.
20 S. Bai, N. Zhang, C. Gao and Y. Xiong, *Nano Energy*, 2018, **53**, 296–336.
21 X. Wang, M. Sun, M. Murugananthan, Y. Zhang and L. Zhang, *Appl. Catal., B*, 2020, **260**, 118205.
22 M. Sun, X. Wang, Z. Chen, M. Murugananthan, Y. Chen and Y. Zhang, *Appl. Catal., B*, 2020, **273**, 119061.
23 H. Zhou, X. Zou and Y. Zhang, *Electrochim. Acta*, 2016, **192**, 259–267.

24 J. Zhang, J. Liu, L. Xi, Y. Yu, N. Chen, S. Sun, W. Wang, K. M. Lange and B. Zhang, *J. Am. Chem. Soc.*, 2018, **140**, 3876–3879.
25 J. P. Desclaux, *At. Data Nucl. Data Tables*, 1973, **12**, 311–406.
26 J. Cai, X. Wu, S. Li and F. Zheng, *ACS Sustainable Chem. Eng.*, 2016, **4**, 1581–1590.
27 H. Zhang, S. Zuo, M. Qiu, S. Wang, Y. Zhang, J. Zhang and X. Lou, *Sci. Adv.*, 2020, **6**, eabb9823.
28 S. Wang, L. Pan, J.-J. Song, W. Mi, J.-J. Zou, L. Wang and X. Zhang, *J. Am. Chem. Soc.*, 2015, **137**, 2975–2983.
29 Y. Zhang, L. Guo, L. Tao, Y. Lu and S. Wang, *Small Methods*, 2019, **3**, 1800406.
30 H. Zhou and Y. Zhang, *J. Phys. Chem. C*, 2014, **118**, 5626–5636.
31 K. Li, S. Gao, Q. Wang, H. Xu, Z. Wang, B. Huang, Y. Dai and J. Lu, *ACS Appl. Mater. Interfaces*, 2015, **7**, 9023–9030.
32 G. Wang, Y. Ling, H. Wang, X. Yang, C. Wang, J. Z. Zhang and Y. Li, *Energy Environ. Sci.*, 2012, **5**, 6180–6187.
33 J.-J. Li, B. Weng, S.-C. Cai, J. Chen, H.-P. Jia and Y.-J. Xu, *J. Hazard. Mater.*, 2018, **342**, 661–669.
34 G. Liu, J. Han, X. Zhou, L. Huang, F. Zhang, X. Wang, C. Ding, X. Zheng, H. Han and C. Li, *J. Catal.*, 2013, **307**, 148–152.
35 T. Pauporté, Y. Soldo-Olivier and R. Faure, *J. Phys. Chem. B*, 2003, **107**, 8861–8867.
36 T. Hsiung, H. Wang and H. Lin, *J. Phys. Chem. Solids*, 2008, **69**, 383–385.
37 A. Makdee, K. C. Chanapattharapol, P. Kidkhunthod, Y. Poo-arporn and T. Ohno, *RSC Adv.*, 2020, **10**, 26952–26971.
38 G. Song, W. Gong, S. Cong and Z. Zhao, *Angew. Chem., Int. Ed.*, 2021, **60**, 5505–5511.
39 A. Agrawal, S. H. Cho, O. Zandi, S. Ghosh, R. W. Johns and D. J. Milliron, *Chem. Rev.*, 2018, **118**, 3121–3207.
40 A. Ziashahabi and T. Ghodselahi, *J. Phys. Chem. Solids*, 2013, **74**, 929–933.
41 X. Chen, L. Liu and F. Huang, *Chem. Soc. Rev.*, 2015, **44**, 1861–1885.
42 G. Xu, H. Zhang, J. Wei, H.-X. Zhang, X. Wu, Y. Li, C. Li, J. Zhang and J. Ye, *ACS Nano*, 2018, **12**, 5333–5340.
43 X. Fang, Q. Shang, Y. Wang, L. Jiao, T. Yao, Y. Li, Q. Zhang, Y. Luo and H. L. Jiang, *Adv. Mater.*, 2018, **30**, 1705112.
44 L. Shi, T. Wang, H. Zhang, K. Chang, X. Meng, H. Liu and J. Ye, *Adv. Sci.*, 2015, **2**, 1500006.
45 H. Zhang, P. Zhang, M. Qiu, J. Dong, Y. Zhang and X. Lou, *Adv. Mater.*, 2019, **31**, 1804883.
46 Z. Yin, B. Liu, S. Fan, P. Wang, X. Wang, D. Long, L. Zhang, X. Yang and X. Li, *Catal. Commun.*, 2019, **130**, 105754.
47 A. Mahmood, X. Wang, X. Xie and J. Sun, *J. Environ. Chem. Eng.*, 2021, **9**, 105069.
48 X. Zou, Y. Dong, X. Zhang and Y. Cui, *Appl. Surf. Sci.*, 2016, **366**, 173–180.
49 K. Zhang, L. Dai, Y. Liu, J. Deng, L. Jing, K. Zhang, Z. Hou, X. Zhang, J. Wang and Y. Feng, *Appl. Catal., B*, 2020, **279**, 119372.
50 C. T. Nguyen, N. Q. Tran, S. Seo, H. Hwang, S. Oh, J. Yu, J. Lee, T. A. Le, J. Hwang and M. Kim, *Mater. Today*, 2020, **35**, 25–33.
51 Y. H. Kim, S. Y. Lee, H. N. Umh, H. D. Song, J. W. Han, J. W. Choi and J. Yi, *ACS Appl. Mater. Interfaces*, 2020, **12**, 15239–15245.
52 F. He, A. Meng, B. Cheng, W. Ho and J. Yu, *Chin. J. Catal.*, 2020, **41**, 9–20.
53 H. Gao, P. Zhang, J. Zhao, Y. Zhang, J. Hu and G. Shao, *Appl. Catal., B*, 2017, **210**, 297–305.
54 S. Meng, W. Sun, S. Zhang, X. Zheng, X. Fu and S. Chen, *J. Phys. Chem. C*, 2018, **122**, 26326–263362.